Automotive Innovation (2021) 4:227–237
https://doi.org/10.1007/s42154-021-00141-5

Study of Longitudinal–Vertical Dynamics for In-Wheel Motor-Driven Electric Vehicles

Yechen Qin[1] · Ze Zhao[1] · Zhenfeng Wang[2] · Guofa Li[3]

Received: 29 April 2020 / Accepted: 8 February 2021 / Published online: 20 April 2021

Abstract

The in-wheel motor (IWM)-driven electric vehicles (EVs) attract increasing attention due to their advantages in dimensions and controllability. The majority of the current studies on IWM are carried out with the assumption of an ideal actuator, in which the coupling effects between the non-ideal IWM and vehicle are ignored. This paper uses the braking process as an example to investigate the longitudinal–vertical dynamics of IWM-driven EVs while considering the mechanical–electrical coupling effect. First, a nonlinear switched reluctance motor model is developed, and the unbalanced electric magnetic force (UEMF) induced by static and dynamic mixed eccentricity is analyzed. Then, the UEMF is decomposed into longitudinal and vertical directions and included in the longitudinal–vertical vehicle dynamics. The coupling dynamics are demonstrated under different vehicle braking scenarios; numerical simulations are carried out for various road grades, road friction, and vehicle velocities. A novel dynamics vibration absorbing system is adopted to improve the vehicle dynamics. Finally, the simulation results show that vehicle vertical dynamic performance is enhanced.

Keywords Mechanical–electrical coupling · Longitudinal–vertical dynamics · In-wheel motor · Suspension system

Abbreviations

CCC	Current chopping control
DVAS	Dynamics vibration absorbing system
EV	Electric vehicle
HBS	Hydraulic braking system
IWM	In-wheel motor
RS	Rattle space
SMA	Sprung mass acceleration
SRM	Switched reluctance motor
TD	Tire deflection
UEMF	Unbalanced electric magnetic force

1 Introduction

Ever stringent emission regulations and higher customer requirements fuel the development of electric vehicles (EVs) with improved dynamic performance [1]. When compared with EVs with a centrally driven motor, the distributed driven configuration has several advantages, such as shorter time delay, more flexible structure, lower vehicle body occupancy, and improved controllability [2].

In-wheel motor (IWM) is the core component of a distributed driven EV; its dynamic characteristics have a significant influence on vehicle performance. A large number of studies on applications of IWM have been carried out in the last decade, mostly focusing on vehicle dynamics control [3–5]. Among those, lateral stability [6], traction/braking [7], and path tracking for autonomous vehicles [8] draw special attention. Both theoretical and experimental results have revealed that over-actuated configuration could significantly improve vehicle dynamics, providing a satisfactory level of fault tolerance.

However, the majority of current studies treat IWM as an ideal actuator, which is far from reality. The mechanical–electrical coupling between the IWMs and suspension causes much more complex dynamic characteristics than the traditional internal engine system. The unattenuated

✉ Guofa Li
hanshan198@gmail.com

[1] School of Mechanical Engineering, Beijing Institute of Technology, Beijing 100081, China

[2] CATARC (Tianjin) Automotive Engineering Research Institute Co., Ltd, Tianjin 300300, China

[3] Institute of Human Factors and Ergonomics, College of Mechatronics and Control Engineering, Shenzhen University, Shenzhen 518060, China

vibration induced by the road unevenness results in a more severe vehicle system response. Tan et al. [9] developed a model for the permanent magnet synchronous motor (PMSM). They observed a 5% difference in vertical and lateral responses when the magnetic force from IWM was considered. Mao et al. [10, 11] studied the influence of torque ripple and rotor position error on the vehicle longitudinal vibration. An electric wheel system model was built based on the Kelvin-Voigt and brush model; experimental results have shown that non-ideal IWM dynamics result in unneglectable vibration between 50 and 100 Hz. As for vehicle vertical dynamics, Sun et al. [12] and Li et al. [13] investigated the relationship between the driving conditions and vehicle responses. The simulation results based on a switched reluctance motor (SRM) have shown that an increase in vehicle velocity in combination with worsening road conditions causes more severe vehicle vertical responses. Qin et al. [14, 15] presented a novel dynamics vibration absorbing system (DVAS), optimizing the IWM coupling effect between vehicle suspension and unbalanced electric magnetic force (UEMF). Based on the above research, it can be concluded that IWM mechanical–electrical characteristics will considerably affect vehicle dynamics.

As a critical vehicle module, the braking system can reduce the vehicle velocity by converting vehicle kinetic energy to heat. The most commonly used anti-lock braking system (ABS) prevents the rotating wheel from locking status, thus shortening the braking distance [16]. A significant number of published papers studied the slip ratio control, road friction estimation, and longitudinal–vertical coupled dynamics [7, 17, 18]. Currently, the research is mainly focused on the synthetization of braking torque and a hydraulic braking system (HBS), or coordinate control between the HBS and IWM for improved regenerative braking efficiency [19]. However, the IWM mechanical–electrical characteristics and longitudinal–vertical coupling effects are seldom discussed in the context of the vehicle braking system for IWM-driven EVs. Since various driving conditions affect both the IWM and braking systems, it is necessary to conduct a thorough study on the braking dynamics of IWM-driven EVs while considering mechanical–electrical coupling.

This paper focuses on longitudinal–vertical and mechanical–electrical coupling braking dynamics for IWM-driven EVs. The UEMF is decomposed into vertical and longitudinal components. The influences of road grade, road friction conditions, and vehicle velocity on the longitudinal–vertical dynamics are thoroughly discussed. The innovations described by this paper can be summarized as:

1. Based on IWM mechanical–electrical coupling characteristics, both longitudinal and vertical UEMF are modeled for the motor with static and dynamic mixed-eccentricity, contributing to a better understanding of vehicle longitudinal–vertical dynamics.
2. The influence of the coupling characteristics on vehicle braking dynamics is investigated, and a novel DVAS is adopted to improve vehicle dynamic responses.

The paper is organized as follows: First, a longitudinal–vertical quarter vehicle model and DVAS are introduced in Sect. 2. The nonlinear SRM modeling and braking dynamics analysis are presented in Sect. 3. The coupling effect and the simulation results are discussed in Sect. 4. Lastly, Sect. 5 concludes the paper and describes the future work.

2 System Modeling

This section covers the development of a vertical–longitudinal coupled quarter vehicle model, novel DVAS structure, and road friction definition.

2.1 Vehicle Longitudinal–Vertical Coupled Model

A longitudinal–vertical coupled model for a quarter vehicle with IWM is shown in Fig. 1. In Fig. 1, m_b is the sprung mass; m_{s1} is the total mass of knuckle, axle and tire; m_s is the stator mass; m_r is the rotor and disc mass; m_{sa} is the stator, axle, and wheel mass; m_{wa} is the rotor and tire mass; k_s is the suspension stiffness; k_t is the tire stiffness; k_d is the absorber stiffness; c_s is the suspension damping; k_{sa} and k_b are the bearing stiffness; c_d is the absorber damping; F_d is the UEMF. This also applies to Fig. 2.

According to Newton's second law, the model dynamics can be described by Eq. (1):

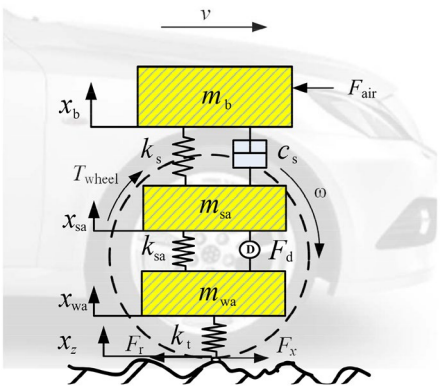

Fig. 1 Vertical–longitudinal vehicle dynamics

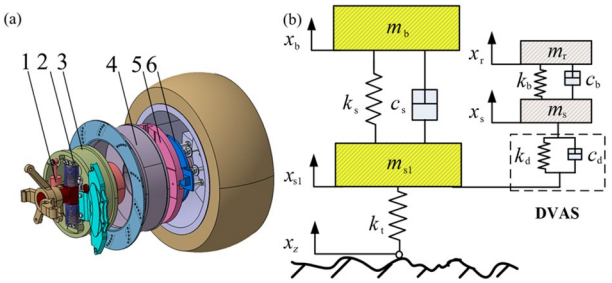

Fig. 2 DVAS-based IWM-suspension systems: **a** explosion view, **b** dynamics structure

$$\begin{cases} \left(m_{\mathrm{b}}+m_{\mathrm{sa}}+m_{\mathrm{wa}}\right)\cdot\dot{v}=F_x-F_{\mathrm{r}}-F_{\mathrm{air}} \\ J\cdot\dot{\omega}=T_{\mathrm{wheel}}-R_{\mathrm{e}}\cdot F_x \\ m_{\mathrm{b}}\ddot{x}_{\mathrm{b}}+k_{\mathrm{s}}\left(x_{\mathrm{b}}-x_{\mathrm{sa}}\right)+c_{\mathrm{s}}\left(\dot{x}_{\mathrm{b}}-\dot{x}_{\mathrm{sa}}\right)=0 \\ m_{\mathrm{sa}}\ddot{x}_{\mathrm{sa}}+k_{\mathrm{s}}\left(x_{\mathrm{sa}}-x_{\mathrm{b}}\right)+c_{\mathrm{s}}\left(\dot{x}_{\mathrm{sa}}-\dot{x}_{\mathrm{b}}\right) \\ +k_{\mathrm{sa}}\left(x_{\mathrm{sa}}-x_{\mathrm{wa}}\right)+F_{\mathrm{d}}=0 \\ m_{\mathrm{wa}}\ddot{x}_{\mathrm{wa}}+k_{\mathrm{t}}\left(x_{\mathrm{wa}}-x_z\right)+k_{\mathrm{sa}}\left(x_{\mathrm{wa}}-x_{\mathrm{sa}}\right)-F_{\mathrm{d}}=0 \end{cases} \tag{1}$$

Regarding the longitudinal dynamics, R_{e} is tire rolling effective radius, J is the wheel moment of inertia, ω is wheel angular velocity, and v is vehicle longitudinal velocity. Furthermore, T_{wheel} is IWM output torque, F_{r} is the force due to rolling resistance, F_{air} is air resistance, and F_x is the longitudinal tire force. The slip ratio λ during braking is defined as:

$$\lambda=\frac{v-\omega R_{\mathrm{e}}}{v} \tag{2}$$

where $\lambda\in[0,1]$, and $\lambda=1$ means that the wheel is locked. The coupling effect can be understood from both longitudinal and vertical directions. For vertical dynamics, the road unevenness induces airgap variation, i.e., $x_{\mathrm{sa}}-x_{\mathrm{wa}}$. Such displacement results in UEMF, which influences both sprung mass and unsprung mass responses. Meanwhile, the longitudinal tire force leads to the coupling effect between vertical and longitudinal directions due to the varying vertical tire load.

2.2 Dynamics Vibration Absorbing System Model

In order to reduce the vibration caused by the coupling effect, the DVAS-based IWM system was proposed and validated using a multi-body software in Ref. [14]. The vertical model of the IWM-suspension coupled system is shown in Fig. 2 [15, 20], where part 1 is the DVAS damper; part 2 is the DVAS spring; part 3 is the stator; part 4 is the rotor; part 5 is the middle plate; part 6 is the transmission plate.

The dynamic equations for DVAS-based system are given as

Table 1 Road condition constants

Road type	c_1	c_2	c_3	λ^*
Dry asphalt	1.28	23.99	0.52	0.17
Wet asphalt	0.86	33.82	0.35	0.12
Dry concrete	1.37	6.46	0.67	0.16
Cobble wet	0.40	33.71	0.12	0.12
Cobble dry	1.20	25.17	0.54	0.40
Snow	0.19	94.13	0.06	0.07
Ice	0.05	306.39	0	0.04

$$\begin{cases} m_{\mathrm{b}}\ddot{x}_{\mathrm{b}}+k_{\mathrm{s}}\left(x_{\mathrm{b}}-x_{\mathrm{s1}}\right)+c_{\mathrm{s}}\left(\dot{x}_{\mathrm{b}}-\dot{x}_{\mathrm{s1}}\right)=0 \\ m_{\mathrm{r}}\ddot{x}_{\mathrm{r}}+k_{\mathrm{b}}\left(x_{\mathrm{r}}-x_{\mathrm{s}}\right)+c_{\mathrm{b}}\left(\dot{x}_{\mathrm{r}}-\dot{x}_{\mathrm{s}}\right)=0 \\ m_{\mathrm{s}}\ddot{x}_{\mathrm{s}}+k_{\mathrm{d}}\left(x_{\mathrm{s}}-x_{\mathrm{s1}}\right)+k_{\mathrm{b}}\left(x_{\mathrm{s}}-x_{\mathrm{r}}\right) \\ +c_{\mathrm{d}}\left(\dot{x}_{\mathrm{s}}-\dot{x}_{\mathrm{s1}}\right)+c_{\mathrm{b}}\left(\dot{x}_{\mathrm{s}}-\dot{x}_{\mathrm{r}}\right)=0 \\ m_{\mathrm{s1}}\ddot{x}_{\mathrm{s1}}+k_{\mathrm{t}}\left(x_{\mathrm{s1}}-x_z\right)+k_{\mathrm{s}}\left(x_{\mathrm{s1}}-x_{\mathrm{b}}\right) \\ +c_{\mathrm{s}}\left(\dot{x}_{\mathrm{s1}}-\dot{x}_{\mathrm{b}}\right)+k_{\mathrm{d}}\left(x_{\mathrm{s1}}-x_{\mathrm{s}}\right) \\ +c_{\mathrm{d}}\left(\dot{x}_{\mathrm{s1}}-\dot{x}_{\mathrm{s}}\right)=0 \end{cases} \tag{3}$$

where x_*, $\dot{x}_*$, and $\ddot{x}_*$ represent displacement, velocity, and acceleration, respectively.

2.3 Road Definition

The road profile and friction models are provided next. The tire-road adhesion force F_x is expressed as

$$\begin{aligned} F_x&=\mu(\lambda)F_Z \\ F_Z&=(m_{\mathrm{b}}+m_{\mathrm{w}})g \end{aligned} \tag{4}$$

where μ is tire–road adhesion coefficient, λ is wheel slip ratio that is defined as

$$\mu(\lambda)=c_1\left(1-e^{-c_2\lambda}\right)-c_3\lambda \tag{5}$$

where the constants c_1, c_2, and c_3 define road friction conditions (see Table 1). The rightmost column of Table 1 is the reference slip ratio λ^*, which shows the slip ratio at which the highest friction coefficient appears.

The statistical features of vertical road profiles are described using power spectral density (PSD). The harmonic superposition algorithm is used to generate the time-domain road profile [21, 22]:

$$q(t)=\sum_{K=1}^{M}\sqrt{2\cdot G_{\mathrm{q}}\left(f_{\mathrm{mid}\text{-}K}\right)\cdot\frac{f_2-f_1}{M}}\sin\left(2\pi f_{\mathrm{mid}\text{-}K}t+\phi_K\right) \tag{6}$$

where $q(t)$ is the generated road profile, $f_{\mathrm{mid}\text{-}K}$ is the kth middle frequency, and $G_{\mathrm{q}}(f_{\mathrm{mid}\text{-}K})$ represents the PSD at $f_{\mathrm{mid}\text{-}K}$. Variable Φ_K is an identically distributed phase in the $(0, 2\pi)$

range. The upper and lower time-domain frequency boundaries are denoted as f_1 and f_2.

3 Switched Reluctance Motor Modeling and Analysis

Modern commercially available IWMs include the induction motor (IM), SRM, and PMSM. The SRM has the advantage of simple structure and fault tolerance and has no winding or permanent magnets [14]. Thus, it is a strong candidate in the mass production of EVs, especially for commercial vehicles. Aiming to further investigate the mechanical–electrical coupling of both the IWM and suspension system, a nonlinear SRM model based on the Fourier series [23] is presented. Additional details and the calculation of longitudinal and vertical UEMF under mixed-eccentricity are provided next. Lastly, the SRM braking dynamics is analyzed.

3.1 Fourier-Series-Based Switched Reluctance Motor Model

A 5-kW exterior rotor SRM prototype with 8/6-four phases [24] is used. It is established that the magnetic co-energy $W(i, \theta)$ is determined by current i and phase inductance $L(\theta, i)$, where θ is the rotor angle. The first three terms of $L(\theta, i)$ Fourier expansion can be written as

$$\begin{aligned} L(\theta, i) = L_0(i) &+ L_1(i)\cos\left(N_r\theta + \pi\right) \\ &+ L_2(i)\cos\left(2N_r\theta + 2\pi\right) \end{aligned} \tag{7}$$

where L_0, L_1, and L_2 are calculated as

$$\begin{cases} L_0(i) = \frac{1}{2}\left[\frac{1}{2}\left(L_a(i) + L_u\right) + L_m(i)\right] \\ L_1(i) = \frac{1}{2}\left(L_a(i) - L_u\right) \\ L_2(i) = \frac{1}{2}\left[\frac{1}{2}\left(L_a(i) + L_u\right) - L_m(i)\right] \end{cases} \tag{8}$$

In Eq. (8), L_a, L_u, and L_m are the inductance at fully aligned ($\theta = 30°$), unaligned ($\theta = 0°$), and mid-way position, respectively. These parameters can be fitted by polynomials as per FEA or experiment results; the resulting function used for the adopted prototyping SRM is shown in Fig. 3a. It can be seen that the fitted inductance function properly describes the reference data. The static phase inductance calculated according to Eq. (7) is shown in Fig. 3b. Considering the relationship between the flux and inductance and by combining Eqs. (7) and (8), the kth phase flux linkage can be expressed as

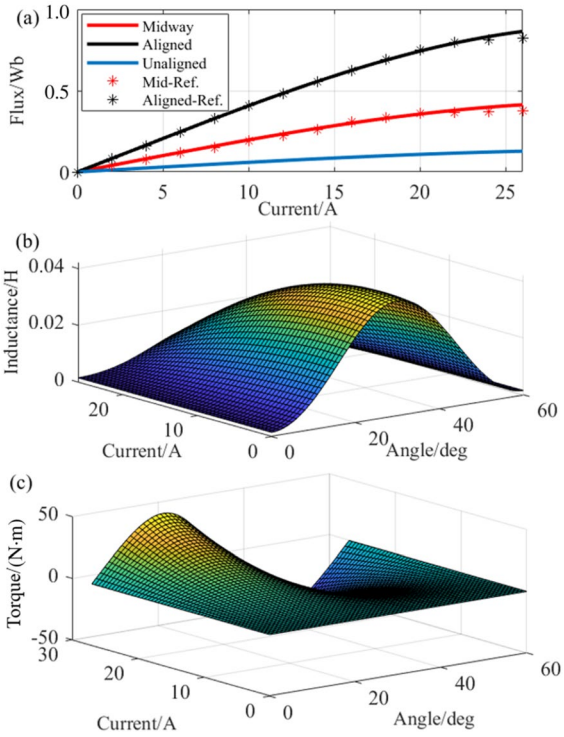

Fig. 3 SRM static characteristics: **a** flux linkage fitting results, **b** phase inductance, **c** phase torque

$$\begin{aligned} \psi\left(\theta, i_k\right) &= \int_0^{i_k} L\left(i_k, \theta\right) \mathrm{d}i_k \\ &= \frac{1}{2}\left[\cos^2\left(N_r\theta\right) - \cos\left(N_r\theta\right)\right] \sum_{n=0}^{N} c_n i^n \\ &+ \sin^2\left(\mathrm{N_r\theta}\right) \sum_{n=0}^{\mathrm{N}} \mathrm{d}_n i^n \\ &+ \frac{1}{2} L_u i_k \left[\cos^2\left(N_r\theta\right) + \cos\left(N_r\theta\right)\right] \end{aligned} \tag{9}$$

where $c_n = a_{n-1}/n$ and $d_n = b_{n-1}/n$. According to Faraday's law, the phase voltage can be written as

$$U_k = R_k i_k + \frac{\mathrm{d}\psi_k}{\mathrm{d}t} = R_k i_k + L_k\left(\theta, i_k\right)\frac{\mathrm{d}i_k}{\mathrm{d}t} + w\frac{\partial \psi_k}{\partial \theta} \tag{10}$$

where w is rotor angular velocity. The phase current can thus be expressed as per Eq. (11):

$$i_k = \int \frac{U_k - R_k i_k - w\frac{\partial \psi_k}{\partial \theta}}{L_k\left(\theta, i_k\right)} \mathrm{d}t \tag{11}$$

For constant phase current i, the relationships between magnetic co-energy $W(i, \theta)$ and torque T and radial force F_r are given as:

$$T = \left.\frac{\partial W(\theta, i)}{\partial \theta}\right|_{i=\text{const}}, \; F_r = \left.\frac{\partial W(\theta, i)}{\partial l_g}\right|_{i=\text{const}} \tag{12}$$

where l_g is the air gap between the rotor and stator. The phase torque can thus be found using

$$\begin{aligned} T_k &= \left.\frac{\partial W(\theta, i)}{\partial \theta}\right|_{i=\text{const}} = \int_0^{i_k} \frac{\partial \psi(\theta, i_k)}{\partial \theta} \, \mathrm{d}i_k \\ &= \sin(N_r \theta) \sum_{n=1}^{N} \frac{1}{n} e_{n-1} i_k^n \\ &\quad + \sin(2N_r \theta) \sum_{n=1}^{N} \frac{1}{n} f_{n-1} i_k^n \end{aligned} \tag{13}$$

where both e and f are intermediate functions. The former, e, can be expressed as $e_n = (1/2)N_r c_n$, and $e_0 = 0$, $e_1 = (1/2)N_r(c_1 - L_u)$. The latter, f, is written as $f_n = N_r d_n - e_n$, and $f_0 = 0$, $f_1 = (1/2)N_r(2d_1 - c_1 - L_u)$. The phase static torque output is shown in Fig. 3c as per Eq. (13). As shown in Fig. 3c, by changing the turn-on angle, SRM can be switched to braking mode and synthesize the negative braking torque.

3.2 Longitudinal and Vertical Unbalanced Electric Magnetic Force

Based on phase torque T_k, the radial force of kth phase can be calculated according to Ref. [25]:

$$F_{rk} = -\frac{T_k \delta}{l_g} \tag{14}$$

where δ is the overlap between rotor and stator. It can be seen from Eq. (14) that the existence of nonzero l_g, also known as eccentricity, will result in the UEMF; the UEMF is defined as the radial force difference between the two opposite stator poles. The eccentricity is caused by several reasons, including manufacturing imprecision and dynamics coupling effect [26]. The air gap eccentricity l_g can be decomposed into x and y-axis, with resulting components expressed as ε_x and ε_y. This paper uses both dynamic and static eccentricity ε_x to represent the air gap in the x-direction, which is caused by the shaft bow, bearing tolerance, and longitudinal road input. The dynamic eccentricity in the y-direction, defined as ε_y, represents the dynamics coupling effect of suspension, IWM, and road unevenness. The relationship between the UEMF F_r, its components, i.e., F_{uv} and F_{ul}, and mixed-eccentricity, is depicted in Fig. 4.

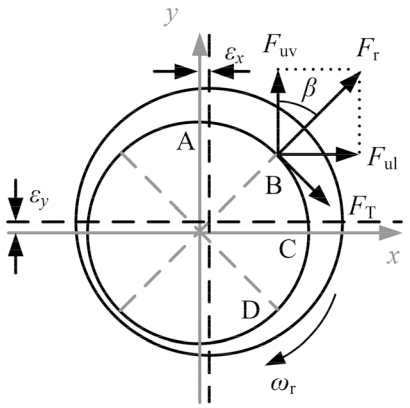

Fig. 4 Vertical and longitudinal UEMF induced by eccentricity

Based on the UEMF definition and mixed-eccentricity, the vertical UEMF F_{uv} can be calculated as [14]:

$$F_{uv} = \sum_{k=1}^{4} \left[\left(-\frac{T_k \delta}{l_g - \varepsilon_y \cos \beta_k} + \frac{T_k \delta}{l_g + \varepsilon_y \cos \beta_k} \right) \cos \beta_k \right] \tag{15}$$

Similarly, the longitudinal UEMF F_{ul} is given as:

$$F_{ul} = \sum_{k=1}^{4} \left[\left(\frac{T_k \delta}{l_g - \varepsilon_x \sin \beta_k} - \frac{T_k \delta}{l_g + \varepsilon_x \sin \beta_k} \right) \sin \beta_k \right] \tag{16}$$

where β is phase structure angle ($\beta_1 = 0°$, $\beta_2 = 45°$, $\beta_3 = 90°$, and $\beta_4 = 135°$), and the nominal air gap is 0.8 mm. Based on Eqs. (15) and (16), it can be concluded that greater torque and eccentricity will result in significant UEMF in both the vertical and longitudinal directions.

3.3 Switched Reluctance Motor Braking Dynamics

Conventional vehicles rely on a mechanical braking system for deceleration, which converts the vehicle kinetic energy to heat energy. Such a conversion results in considerable energy loss; previous research revealed that in heavy urban-road conditions, potentially more than 60% of braking energy could be recovered. If properly used, this amount of energy could improve fuel efficiency by 19% to 40% [27]. In contrast to conventional mechanical braking systems, the application of IWM enables regenerative braking.

The SRM briefly achieves negative torque by exciting phase windings as the inductance decreases, allowing the energy to be stored for charging a battery or being reused [28]. The synthesized negative torque can also be achieved by tuning both the turn-on angle θ_{on} and turn-off angle θ_{off}. It should be noted that improper angle settings will result in positive torque output, dramatically reducing the braking efficiency.

For this reason, the influence of θ_{on} and θ_{off} on the SRM characteristics should be further discussed to ensure efficient and stable braking torque output. The well-known current chopping control (CCC) is adopted to avoid the stator winding resistance from consuming electrical energy. The preset current limit is 23 A. According to the configuration of the adopted SRM model, the given θ_{on} range is between 22° and 34°, while the θ_{off} range is between 52° and 60°. Since the main purpose of SRM braking is to provide a stable braking torque (fewer fluctuations), the braking torque mean value $T_{b\text{-}mean}$ and standard deviation $T_{b\text{-}std}$ are used as the indexes. (The results are shown in Fig. 5.) It can be seen that θ_{on} value is around 30°, which corresponds to a fully aligned position, and a higher θ_{off} results in larger $T_{b\text{-}mean}$ with a smaller $T_{b\text{-}std}$. In this context, the θ_{on} and θ_{off} angle values are selected as 28° and 60°, respectively.

4 Vehicle-Switched Reluctance Motor Coupling Effect

The previous section details the SRM modeling, based on which the UEMF is analytically described. It is concluded that UEMF is affected by eccentricity, torque, and angular speed. Based on the above-presented analysis, this section studies the interactions between IWM and vehicle systems during emergency braking by considering the mechanical–electrical coupling effect. The results are used to compare the vehicle responses for both the DVAS and traditional structures.

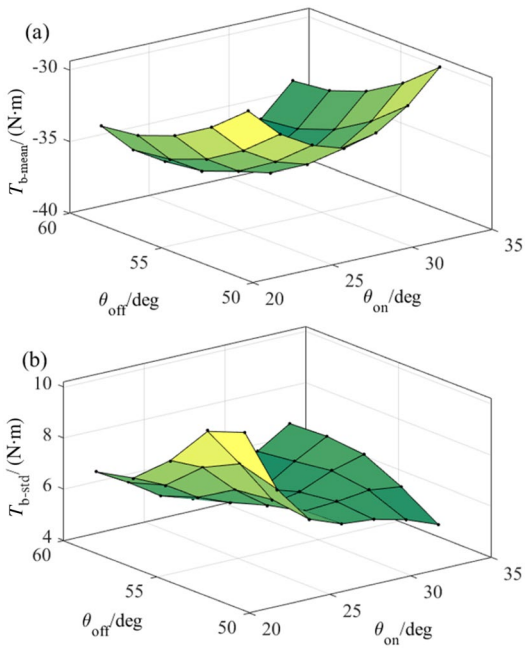

Fig. 5 SRM braking torque characteristics for different turn-on angle and turn-off angles: **a** Mean value, **b** Standard deviation

4.1 Coupling Effect and Simulation Setting

Based on the models presented in Sects. 2 and 3, the obtained dynamics coupling effects in the braking process along with the corresponding equations are shown in Fig. 6.

For the studied IWM-suspension system working in braking or traction mode, the external excitations originate from two sources—the air drag force and road input. The latter consists of the vertical unevenness input, rolling resistance, and longitudinal friction tire force. For a given road profile, the longitudinal velocity and spatial road profile determine the vertical road input, which in turn affects the vertical vehicle dynamic load. The vertical vehicle dynamic load, in turn, primarily affects vehicle longitudinal tire force. Finally, the longitudinal tire force determines longitudinal vehicle acceleration and closes the loop. Inside the IWM-suspension system, the wheel speed is affected by the traction/braking torque, the longitudinal UEMF caused by static eccentricity affects the longitudinal dynamics. Similarly, the vertical UEMF caused by an uneven road profile, which is also related to wheel speed, induces high-frequency disturbance to the suspension system.

In the investigated vehicle, the braking torque is provided by both the HBS and IWM. The CCC controller of IWM regulates the phase voltage according to the phase current, as described in Sect. 3.3. As for the HBS, the vehicle control unit (VCU) calculates the wheel slip as shown in Eq. (2) and output slip ratio difference $\lambda - \lambda^*$ in the ABS module during each time step.

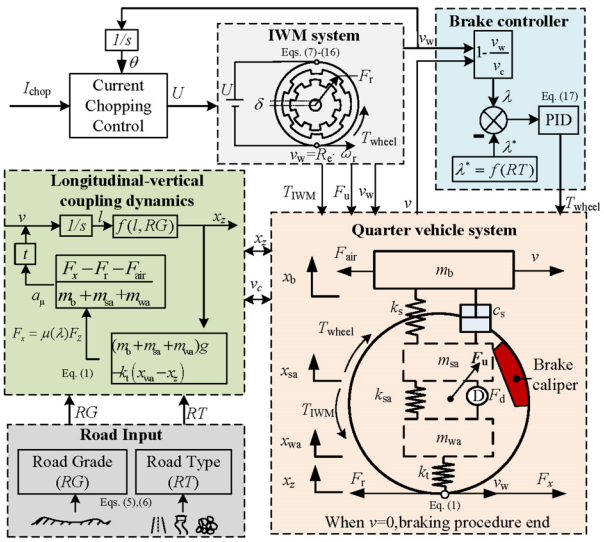

Fig. 6 IWM-suspension longitudinal–vertical coupling

It should be noted that the value of reference slip ratio λ^* is assumed to be known, as many papers have provided the method for λ^* estimation with available vehicle response measurements [17]. A PID controller is applied to determine HBS braking torque T_b, as shown in Eq. (17).

$$T_b = K_P(\lambda - \lambda^*) + K_I \int_0^t (\lambda - \lambda^*)dt + K_D \frac{d(\lambda - \lambda^*)}{dt} \quad (17)$$

where K_P, K_I and K_D are PID controller parameters. The system simulation parameters are given in Table 2 [14, 20]. According to the references above, the parameters were optimized using the particle swarm optimization, while considering system natural frequency and structure dimension constraints. Furthermore, the detailed discussion regarding system structure and implementation can be found in Ref. [14].

To examine the longitudinal–vertical dynamics during the braking process, the following vehicle responses are selected: braking distance S_{bra}, braking duration t_{bra}, sprung mass acceleration (SMA), rattle space (RS), and tire deflection (TD).

4.2 Numerical Simulations

A series of numerical simulations are carried out to illustrate the mechanical–electrical coupling effect of the IWM-suspension system in simulation software by following the structure shown in Fig. 6. The influence of road grade and vehicle velocity is presented first, followed by the demonstration of possible improvements through the DVAS application.

4.2.1 Influence of Road Grade and Velocity

This subsection covers the impact of road grade, road friction condition, and vehicle velocity on the longitudinal–vertical dynamics. The road grades ISO-A and ISO-C are selected, along with the vehicle velocities $v = \{20, 40, 60, 80\}$ km/h. Both dynamic and static eccentricities ε_x are used in the longitudinal direction. The dynamic eccentricity variance equals that of the ε_y, which is marked as $\varepsilon_x(D)$, and the static eccentricities are defined as $\varepsilon_x = \{0, 0.4\}$. The static eccentricity $\varepsilon_x = 0.4$ represents the 40% decentration percentage, and the nominal air gap $x_{sa} - x_{wa}$ is defined to be 0.8 mm. For the sake of simplicity, the road friction condition is taken as dry asphalt and cobblestone; extensive simulations have shown that the vehicle traveling on different road friction conditions has comparable results.

For a vehicle traveling on cobblestone in dry road conditions that suddenly start braking at 40 km/h, the braking torque and tracking performance of slip ratio are shown in Fig. 7. It can be seen that the PID controller synthesizes the braking torque T_b and tracks $\lambda^* = 0.4$ well.

The simulation results for braking distance S_{bra} and braking duration t_{bra} on grade ISO-A road are compared in Figs. 8 and 9. Results obtained from road level ISO-C follow a similar trend. Based on both figures, it can be concluded that increased vehicle velocity results in more extensive S_{bra} and t_{bra}. The braking duration t_{bra} is linearly proportional to the velocity, while braking distance S_{bra} shows the approximate quadratic relationship. As for the nonzero static eccentricity case, approximately 26% and 23% greater braking duration

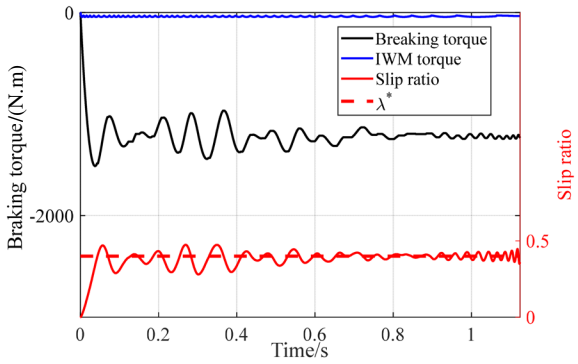

Fig. 7 Braking torque and slip ratio tracking performance by the PID controller

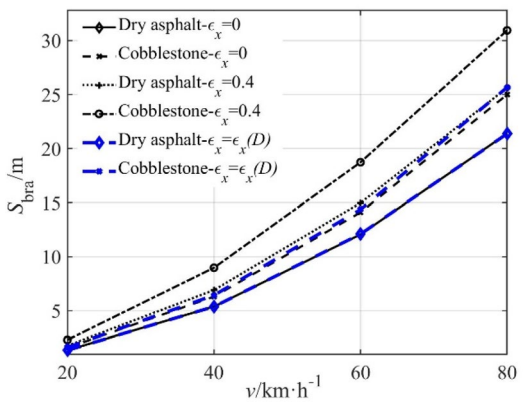

Fig. 8 Braking distance for vehicle traveling on road ISO-A

Table 2 IWM-suspension system parameters

Symbol	Value	Symbol	Value
m_b	332 kg	m_s	20 kg
m_{wa}	40 kg	m_{s1}	25 kg
k_s	15,800 N/m	m_r	25 kg
c_s	1270 N·s/m	k_d	53,000 N/m
k_t	220,000 N/m	c_d	1900 N·s/m
m_{sa}	70 kg	R_e	0.316 m
k_b, k_{sa}	1.4×10^7 N/m	J	0.9 kg·m^2

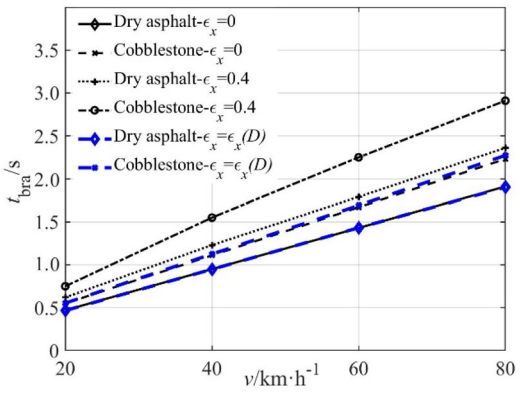

Fig. 9 Braking duration for vehicle traveling on road ISO-A

and 24% and 18% longer braking distance are observed on both the dry asphalt and cobblestone road conditions, respectively. It is evident that a nonzero static eccentricity reduces braking dynamics, while the periodic pulse-like UEMF, which is calculated using Eq. (16), reduces braking force and increases both the S_{bra} and t_{bra}. As for the system with nonzero dynamic eccentricity, the braking performance is almost the same as the zero-eccentricity case, which can be interpreted into that the dynamic eccentricity with zero-mean value has little effect on the longitudinal dynamic in the whole braking process.

The longitudinal UEMFs at 40 and 60 km/h are further compared in Fig. 10a under $\varepsilon_x = 0.4$. It can be seen that both UEMFs have the same amplitude. The case with higher initial vehicle velocity results in a high-frequency UEMF component. The reason for such behavior is that the eccentricity in the longitudinal direction is assumed to be constant, in combination with the braking torque controlled by the CCC controller. Based on Eq. (16), it can be concluded that the overlap angle δ is the determinant factor, and higher vehicle velocity results in a faster phase switching. As for the dynamic eccentricity case shown in Fig. 10b, the slower initial speed results in lower UEMF amplitude, as road excitation energy is proportional to the vehicle velocity.

As for the vertical suspension response, the root mean squares (RMS) of SMA, RS, and TD are compared (see Table 3). In the same table, vertical vehicle responses on dry asphalt road condition are compared for varying velocities and eccentricities. From Table 3a–c, it can be seen

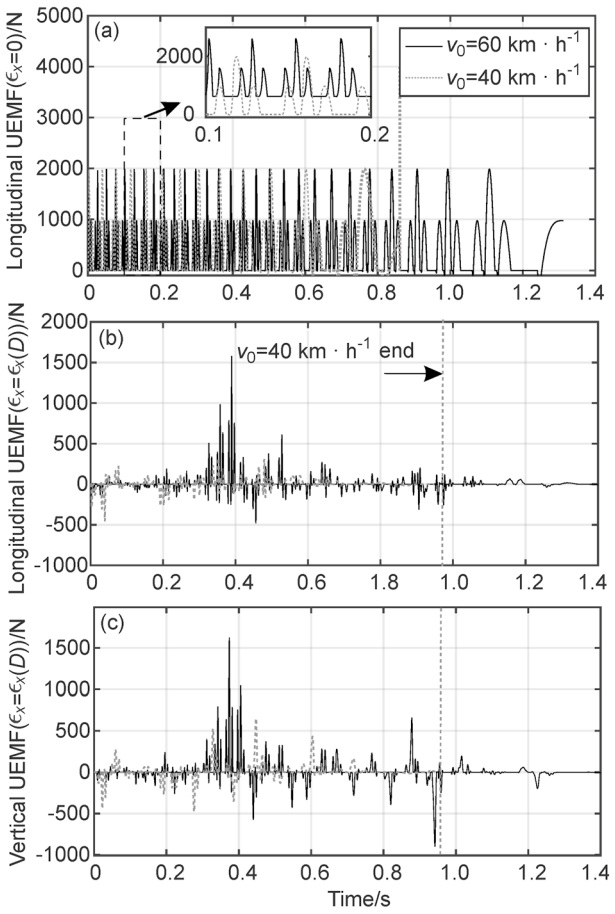

Fig. 10 Longitudinal and vertical UEMF for vehicle driving on ISO A-level road at 40 and 60 km/h, **a** $\varepsilon_x = 0.4$-longitudinal, **b** ε_x (D)-longitudinal, **c** ε_x (D)-vertical

Table 3 Vehicle vertical responses on dry asphalt

v (km/h)	*SMA* (m^2/s)	*RS* (mm)	*TD* (mm)
(a) Dry asphalt, ISO-A, $\varepsilon_x = 0$			
20	0.15	1.32	0.39
40	0.21	2.51	0.57
60	0.26	2.85	0.65
80	0.29	2.98	0.80
(b) Dry asphalt, ISO-A, $\varepsilon_x = \varepsilon_x(D)$			
20	0.15	1.32	0.39
40	0.21	2.51	0.57
60	0.26	2.85	0.65
80	0.29	2.98	0.80
(c) Dry asphalt, ISO-A, $\varepsilon_x = 0.4$			
20	0.15	1.08	0.41
40	0.22	2.18	0.59
60	0.25	2.87	0.62
80	0.31	3.24	0.88
(d) Dry asphalt, ISO-C, $\varepsilon_x = 0$			
20	0.86	6.61	3.24
40	0.91	6.66	3.23
60	0.92	7.29	3.56
80	1.13	8.70	4.33

Table 4 Vehicle vertical responses on cobblestone

v (km/h)	SMA (m^2/s)	RS (mm)	TD (mm)
(a) Cobblestone, ISO-A, $\varepsilon_x = 0$			
20	0.14	1.46	0.38
40	0.22	2.45	0.57
60	0.26	2.72	0.67
80	0.30	3.20	0.79
(b) Cobblestone, ISO-A, $\varepsilon_x = \varepsilon_x(D)$			
20	0.14	1.45	0.38
40	0.22	2.45	0.57
60	0.26	2.72	0.67
80	0.30	3.20	0.80
(c) Cobblestone, ISO-A, $\varepsilon_x = 0.4$			
20	0.15	1.24	0.41
40	0.21	2.44	0.58
60	0.26	2.84	0.65
80	0.29	3.02	0.80

that a velocity increment results in more prominent vehicle responses. However, the differences in vertical vehicle responses for different significant eccentricities are modest. Although the responses at different velocities vary, such a phenomenon can be interpreted as the consequence of the relatively short braking duration and nonstationary responses caused by the decreasing vehicle velocity. Similar results can also be observed in Table 4, in which vertical vehicle responses for different eccentricities are compared under cobblestone road conditions. By comparing Table 3a, d, it is evident that road grade plays an important role in vertical responses; the inferior road quality leads to a more severe SMA, RS, and TD.

4.2.2 Implementation of DVAS

Based on the previous subsection, it can be concluded that the eccentricity greatly influences the vehicle braking dynamics. Furthermore, it is shown that lower-quality road grades, as well as higher velocity, lead to a more prominent vertical response. In this section, the longitudinal–vertical dynamics of the novel DVAS, as modeled by Eq. (3), will be investigated. The simulation results are shown in Table 5.

Regarding the vertical responses shown in the rightmost three columns of Table 5, it can be concluded that the influence of eccentricity on the vertical response is not significant. By comparing Tables 5a and 3d, the improvement on SMA and TD is apparent, meaning that the DVAS can improve passenger feeling and reduce the wheel hop probability. As for the RS, the DVAS case is comparable to the traditional one. The above-presented analysis confirms that the DVAS structure can improve the vertical response during the braking process. The SMA comparison performed on dry asphalt at 60 km/h is shown in Fig. 11. It is evident that DVAS performs better and can effectively reduce SMA between the initial velocity and the full stop.

Regarding the longitudinal braking dynamics, a comparison with the traditional system reveals that the application of the novel DVAS will not reduce either braking duration or braking distance. Furthermore, the longitudinal results are shown in the second and third columns of Table 5 (obtained for a vehicle driving on road grade ISO-C, regardless of eccentricity), which remain practically unchanged when compared with the results given in Figs. 8 and 9. This means that, although the DVAS can lower TD response, the influence of the reduced TD on the longitudinal braking dynamics is unremarkable.

To sum up, the following conclusions can be drawn based on the presented simulation results:

Table 5 DVAS-based vehicle vertical responses on dry asphalt

v (km/h)	t_{bra} (s)	S_{bra} (m)	SMA (m^2/s)	RS (mm)	TD (mm)
(a) Dry asphalt, ISO-C, $\varepsilon_x = 0$					
20	0.47	1.36	0.61	5.03	1.74
40	0.95	5.39	0.72	5.12	2.29
60	1.43	12.09	0.75	6.87	2.88
80	1.91	21.41	0.92	7.10	3.14
(b) Dry asphalt, ISO-C, $\varepsilon_x = \varepsilon_x(D)$					
20	0.47	1.36	0.60	5.03	1.74
40	0.96	5.42	0.72	5.11	2.29
60	1.45	12.21	0.75	6.86	2.88
80	1.95	21.97	0.92	7.10	3.15
(c) Dry asphalt, ISO-C, $\varepsilon_x = 0.4$					
20	0.61	1.78	0.62	6.03	1.71
40	1.24	6.93	0.75	6.12	2.49
60	1.78	15.00	0.72	6.09	2.77
80	2.37	25.66	0.95	7.10	3.20

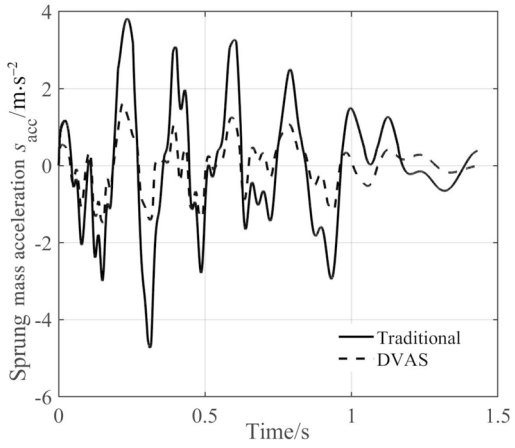

Fig. 11 Comparison of SMA for vehicle driving on dry asphalt at 60 km/h

1. Higher velocity and inferior road grade result in a more prominent vehicle vertical response. The road friction condition is found to have a minor influence.
2. Both the higher velocity and motor eccentricity increase the braking duration and distance. Although the former is well known, the latter is seldom discussed. It mostly originates from the mechanical–electrical coupling effect between the motor and vehicle.
3. The application of DVAS can effectively reduce vehicle SMA and TD. However, its influence on the longitudinal braking dynamics is not apparent.

5 Conclusions

This paper presents an in-depth investigation on the longitudinal–vertical dynamics for in-wheel motor (IWM)-driven EVs considering the mechanical–electrical coupling effect. A nonlinear switched reluctance motor (SRM) model is developed, allowing for a derivation of analytical expressions of both longitudinal and vertical unbalanced electric magnetic force (UEMF). The SRM braking dynamics are also discussed, and a current chopping control (CCC) controller is designed to ensure SRM is working in the braking mode. The coupling effect analysis is followed by numerical simulations for various road levels, road friction conditions, and velocities. The simulation results have shown that road friction has a neglectable influence on the vertical vehicle response in braking scenarios. Dynamics vibration absorbing system (DVAS) is found to simultaneously improve sprung mass acceleration (SMA) and tire deflection (TD) during the braking process. The motor eccentricity is also found to have an important role in longitudinal dynamics; a higher decentration percentage results in diminished braking performance. Future studies will focus on validating the system with high-fidelity software, developing IWM-suspension control strategies while considering the mechanical–electrical coupling effect and investigating motor control strategy to achieve cooperative hydraulic braking system (HBS) control.

Acknowledgements This study is supported by the National Natural Science Foundation of China under Grant 51805028, in part by the Young Elite Scientists Sponsorship Program funded by the China Society of Automotive Engineers, and in part by the Beijing Institute of Technology Research Fund Program for Young Scholars.

Declarations

Conflict of interest On behalf of all authors, the corresponding authors state that there is no conflict of interest.

References

1. Qin, Y., Tang, X., Jia, T., Duan, Z., Zhang, J., Li, Y., Zheng, L.: Noise and vibration suppression in hybrid electric vehicles: state of the art and challenges. Renew. Sustain. Energy Rev. **124**, 109782 (2020)
2. Hu, C., Wang, Z., Qin, Y., Huang, Y., Wang, J., Wang, R.: Lane keeping control of autonomous vehicles with prescribed performance considering the rollover prevention and input saturation. IEEE Trans. Intell. Transp. Syst. (2019). https://doi.org/10.1109/TITS.2019.2924937
3. Chen, Y., Wang, J.: Design and evaluation on electric differentials for overactuated electric ground vehicles with four independent in-wheel motors. IEEE Trans. Veh. Technol. **61**(4), 1534–1542 (2012)
4. Bilgin, B., Liang, J., Terzic, M.V., et al.: Modeling and analysis of electric motors: state-of-the-art review. IEEE Trans. Transp. Electrif. **5**(3), 602–617 (2019)
5. Zhao, J., Wong, P.K., Ma, X., Xie, Z.: Chassis integrated control for active suspension, active front steering and direct yaw moment systems using hierarchical strategy. Veh. Syst. Dyn. **55**(1), 72–103 (2017)
6. Başlamişli, S.Ç., Köse, İE., Anlaç, G.: Handling stability improvement through robust active front steering and active differential control. Veh. Syst. Dyn. **49**(5), 657–683 (2011)
7. Li, W., Du, H., Li, W.: Four-wheel electric braking system configuration with new braking torque distribution strategy for improving energy recovery efficiency. IEEE Trans. Intell. Transp. Syst. (2019). https://doi.org/10.1109/TITS.2018.2888915
8. Guo, J., Luo, Y., Li, K.: An adaptive hierarchical trajectory following control approach of autonomous four-wheel independent drive electric vehicles. IEEE Trans. Intell. Transp. Syst. **19**(8), 2482–2492 (2017)
9. Tan, D., Lu, C.: The influence of the magnetic force generated by the in-wheel motor on the vertical and lateral coupling dynamics of electric vehicles. IEEE Trans. Veh. Technol. **65**(6), 4655–4668 (2015)
10. Mao, Y., Zuo, S., Wu, X., Duan, X.: High frequency vibration characteristics of electric wheel system under in-wheel motor torque ripple. J. Sound Vib. **400**, 442–456 (2017)
11. Mao, Y., Zuo, S., Cao, J.: Effects of rotor position error on longitudinal vibration of electric wheel system in in-wheel PMSM

driven vehicle. IEEE/ASME Trans. Mechatron. **23**(3), 1314–1325 (2018)
12. Sun, W., Li, Y., Huang, J., Zhang, N.: Vibration effect and control of in-wheel switched reluctance motor for electric vehicle. J. Sound Vib. **338**, 105–120 (2015)
13. Li, Z., Zheng, L., Gao, W., Zhan, Z.: Electromechanical coupling mechanism and control strategy for in-wheel-motor-driven electric vehicles. IEEE Trans. Ind. Electron. **66**(6), 4524–4533 (2018)
14. Qin, Y., He, C., Shao, X., et al.: Vibration mitigation for in-wheel switched reluctance motor driven electric vehicle with dynamic vibration absorbing structures. J. Sound Vib. **419**, 249–267 (2018)
15. Qin, Y., Wang, Z., Yuan, K., Zhang, Y.: Comprehensive analysis and optimization of dynamic vibration-absorbing structures for electric vehicles driven by in-wheel motors. Automot. Innov. **2**(4), 254–262 (2019)
16. Savaresi, S.M., Tanelli, M.: Active Braking Control Systems Design for Vehicles. Springer Science & Business Media, Cham (2010)
17. Zhu, Y., Zhao, C., Zhang, J., et al.: Vibration control for electric vehicles with in-wheel switched reluctance motor drive system. IEEE Access **8**, 7205–7216 (2020)
18. Zhang, J., Sun, W., Jing, H.: Nonlinear robust control of antilock braking systems assisted by active suspensions for automobile. IEEE Trans. Control Syst. Technol. **27**(3), 1352–1359 (2018)
19. Hu, K.W., Yi, P.H., Liaw, C.M.: An EV SRM drive powered by battery/supercapacitor with G2V and V2H/V2G capabilities. IEEE Trans. Ind. Electron. **62**(8), 4714–5472 (2015)
20. Xu, B., Xiang, C., Qin, Y., et al.: Semi-active vibration control for in-wheel switched reluctance motor driven electric vehicle with dynamic vibration absorbing structures: concept and validation. IEEE Access **6**, 60274–60285 (2018)
21. Qin, Y., Wang, Z., Xiang, C., et al.: Speed independent road classification strategy based on vehicle response: theory and experimental validation. Mech. Syst. Signal Process. **117**, 653–666 (2019)
22. Qin, Y., Wei, C., Tang, X., et al.: A novel nonlinear road profile classification approach for controllable suspension system: simulation and experimental validation. Mech. Syst. Signal Process. **125**, 79–98 (2019)
23. Khalil, A., Husain, I.: A fourier series generalized geometry-based analytical model of switched reluctance machines. IEEE Trans. Ind. Appl. **43**(3), 673–684 (2007)
24. Xue, X.D., Cheng, K.W.E., Lin, J.K., et al.: Optimal control method of motoring operation for SRM drives in electric vehicles. IEEE Trans. Veh. Technol. **59**(3), 1191–1204 (2010)
25. Krishnan, R.: Switched Reluctance Motor Drives: Modeling, Simulation, Analysis, Design, and Applications. CRC Press, Boca Raton (2017)
26. Ebrahimi, B.M., Faiz, J., Roshtkhari, M.J.: Static-, dynamic-, and mixed-eccentricity fault diagnoses in permanent-magnet synchronous motors. IEEE Trans. Ind. Electron. **56**(11), 4727–4739 (2009)
27. Li, L., Li, X., Wang, X., Liu, Y., Song, J., Ran, X.: Transient switching control strategy from regenerative braking to anti-lock braking with a semi-brake-by-wire system. Veh. Syst. Dyn. **54**(2), 231–257 (2016)
28. Hsieh, M.F., Li, P.Y., Ting, H.Y., et al.: A regenerative braking system for switched reluctance machine applied to electric vehicles. Paper presented at the 19th International Conference on Electrical Machines and Systems, IEEE, Chiba, 13 Nov 2016